

SCIENTIFIC REPORTS



OPEN

Development of chipless, wireless current sensor system based on giant magnetoimpedance magnetic sensor and surface acoustic wave transponder

Vijay V. Kondalkar, Xiang Li, Ikmo Park , Sang Sik Yang & Keekeun Lee

A chipless, wireless current sensor system was developed using a giant magnetoimpedance (GMI) magnetic sensor and one-port surface acoustic wave (SAW) reflective delay line for real-time power monitoring in a current-carrying conductor. The GMI sensor has a high-quality crystalline structure in each layer, which contributes to a high sensitivity and good linearity in a magnetic field of 3–16 Oe. A 400 MHz RF energy generated from the interdigital transducer (IDT)-type reflector on the one-port SAW delay line was used as an activation source for the GMI magnetic sensor. The one-port SAW delay line replaces the presently existing transceiver system, which is composed of thousands of transistors, thus enabling chipless and wireless operation. We confirmed a large variation in the amplitude of the SAW reflection peak with a change in the impedance of the GMI sensor caused by the current flow through the conductor. Good linearity and sensitivity of -0.691 dB/A were observed for currents in the range 1–12 A. Coupling of Mode (COM) modeling and impedance matching analysis were also performed to predict the device performance in advance and these were compared with the experimental results.

In modern electrical technologies, there is a need for a system that monitors the real-time power usage at any location and then transmits the information wirelessly to a portable reader^{1,2}. By monitoring the real-time power usage, unnecessary energy consumption can be prevented, and necessary actions can be taken to prevent any major accident in electric power distribution infrastructures^{3–7}. When an electric car or a household appliance is being charged, there is a need for real-time monitoring of charging status; i.e., whether there is a proper flow of current or any contact failure or aging problem with the charger⁸. In order to realize such a system, current and voltage sensors with high sensitivity and reliability are necessary^{9–12}. Variety of current sensors with different designs and operating mechanisms, which include resistive shunt current sensor, Hall sensor, Inductive sensor, Rogowski coil sensor, have been reported¹³. The resistive shunt sensor, which is based on Ohm's law, measures the current through direct contact with the path of current. It is easy to measure DC and low frequency currents using this sensor; however, it requires complex signal-conditioning circuits and poses heat generation and safety issues^{14,15}. Hall sensor is based on a non-contact method and is relatively safe. However, to measure external current, knowledge of both the magnetic field generated from current-carrying path and the current flowing in the sensor itself is required. In addition, it has problems with low breakdown voltage owing to the use of semiconductor and non-linearity in the measurement of high external currents. The Rogowski coil sensor has a copper wire wound around air or a non-magnetic core and measures the external current by using an integrator at the output terminal^{16–18}. Large size, heaviness, high power consumption, and complex wireless communication technology are critical issues that need to be resolved¹⁹. Current sensors based on GMI and giant magnetoresistance (GMR) have been reported in literature, and are preferred because of their high sensitivity, wide frequency range, small size, low power consumption, and facile compatibility with CMOS technologies^{20–25}. The development of this kind of current sensors has been facilitated by the progress in both theoretical and technological methods

Department of Electrical and Computer Engineering, Ajou University, Woncheon-dong, Yeongtong-gu, Suwon, 443–749, Republic of Korea. Correspondence and requests for materials should be addressed to K.L. (email: keekeun@ajou.ac.kr)

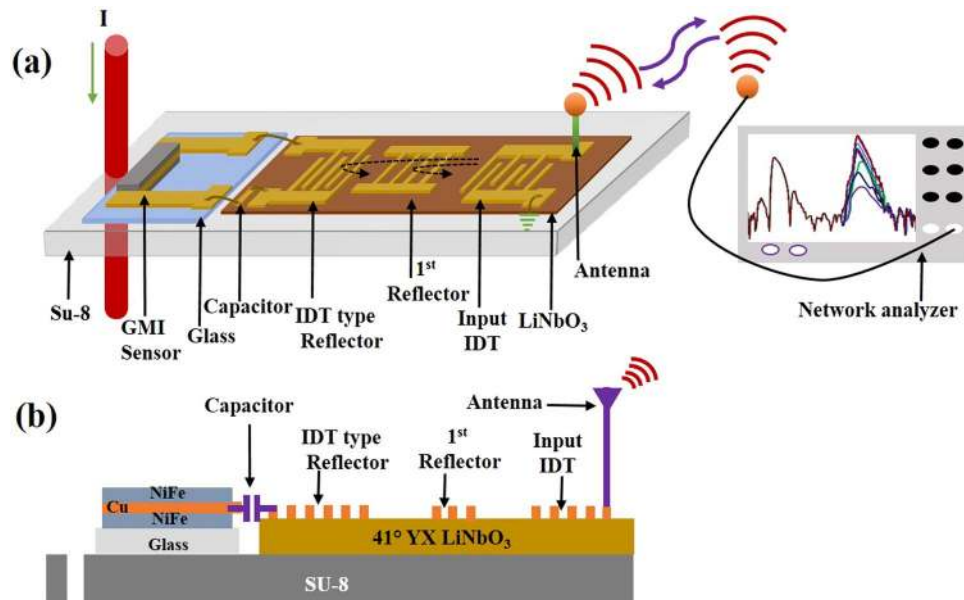


Figure 1. (a) Overall view of the developed chipless, wireless current sensor system. It consists of GMI sensor, one-port SAW delay line, impedance matching element, clip-on packaging platform, antenna, and reader system. (b) Cross-sectional view of sensor system on the clip-on packaging platform.

over several years. Compared to traditional sensors, the GMI and GMR sensors are compatible with many other state-of-the-art technologies^{26,27}.

A wireless transceiver system is required to send the measured current to a remote reader. The currently existing wireless transceiver systems consist of a battery, an antenna, a voltage regulator, an amplifier, a de-modulator, a multiplexer, an A/D converter, and a digital processor^{28–30}. These kinds of wireless systems have several issues including signal distortion and addition of noise when passing the wireless electronic circuits, and heavy re-chargeable battery installation to activate the circuits and current sensor. In addition, the currently existing wireless transceiver systems require signal processing to be performed twice. Signal processing is first fulfilled at the forefront of the wireless system and then again in the distant reader unit. Above all, these systems are expensive, heavy, high power consuming, and difficult to use when multiple sensors are integrated in a single system.

In the recent years, reflective surface acoustic wave devices have been implemented as passive transponders to overcome these drawbacks. Fu *et al.* reported wireless passive SAW sensor by using the single electrode-type IDT structure as reflector and is connected with the external capacitive and resistive sensors as load impedances³¹. Schimetta *et al.* developed a wireless pressure-measurement system with a combination of a SAW reflective delay line with a high-Q capacitive pressure sensor³². Li *et al.* integrated the magnetic fields, temperature, and humidity sensor with a SAW transducer to realize a passive and wireless multifunctional sensor³³. Jung *et al.* developed a wireless neural probe in which the varicap diode interconnected with sharp metal shank was electrically linked to the SAW device³⁴. Karilainen *et al.* developed the voltage sensor for biomedical application based on a SAW delay line with voltage-dependent impedance loading on a reflector IDT³⁵.

We present a chipless, wireless current sensing system that comprises of a GMI magnetic sensor and one-port surface acoustic wave (SAW) delay line. Figure 1 illustrates the overall view of the developed sensor and measurement system. The developed system consists of a GMI magnetic sensor for current sensing, one-port SAW delay line for the chipless and battery-free transceiver system, an impedance matching element for large sensitivity, two antennas, a clip-on packaging platform, and a network analyzer as a reader. When the IDT on the one-port SAW reflective delay line receives an RF energy through the antenna, a SAW generated on the piezoelectric substrate propagates towards the two reflectors. Some of the SAW energy is reflected by the reflectors, and returned to the input IDT and re-converted into EM wave by the transducer this EM wave is transmitted to the distant measurement system through the antenna. There are two reflection peaks at the reader system. The GMI magnetic sensor is connected to the second IDT-type reflector on the one-port SAW reflective delay line. The conductor line carrying the current produces a magnetic field that affects the impedance variation of the GMI; this gives rise to variations in the second reflection peak of the reader unit. By assessing the amplitude changes of the second reflection peak, the data related to the value of current in the conductor can be evaluated. This system possesses many merits over the currently existing wireless current sensor systems: it is chipless and battery-free so it does not require any complex transceiver systems and heavy re-chargeable battery to activate the circuits. The one-port SAW delay line supersedes the currently available transceiver system that consists of a few thousand transistors. A clip-on packaging platform was employed to control the distance, angle, and tilt between the current-carrying conductor and the GMI sensor. Coupling of mode (COM) modeling and impedance matching analysis were performed to predict the optimized structural parameters for the one-port SAW delay line and to make the change in amplitude of the second reflection peak large and linear in terms of the magnitude of the current flowing in the wire.

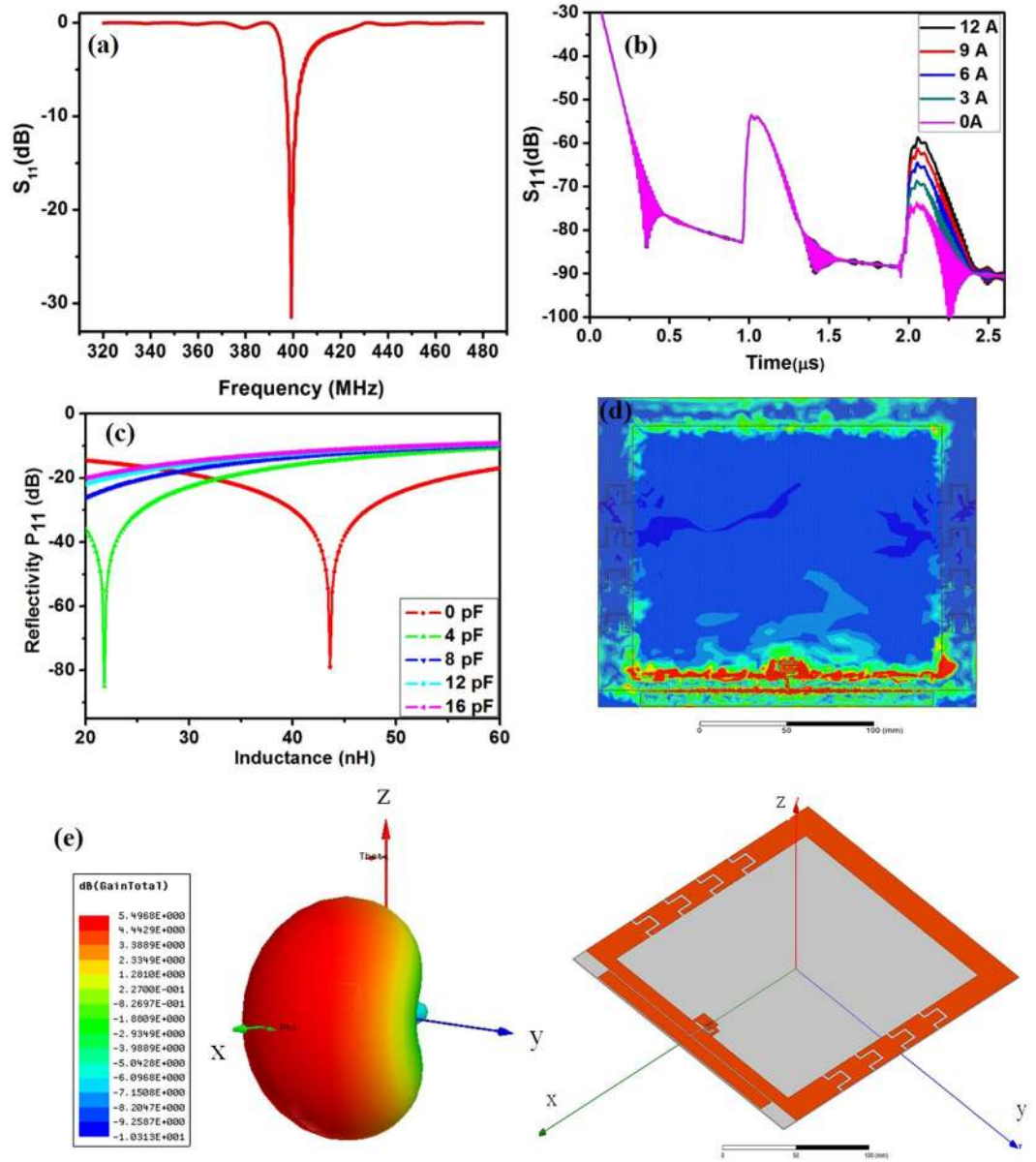


Figure 2. (a) Simulated S_{11} in terms of the frequency for one-port SAW reflective delay line connected with GMI magnetic sensor, (b) Amplitude variations of the second reflection peak in terms of current flowing in conductor line, (c) Simulated results of the reflectivity of P_{11} as a function of the loads, (d) Surface current density on the patch array of the antenna at 400 MHz, (e) 3-D radiation pattern at 400 MHz.

Results and Discussion

Design considerations and analytical modeling.

Chipless, wireless SAW transponder. A one-port SAW reflective delay line was used to supersede the currently available wireless transceiver systems. The one-port SAW reflective delay line consists of input IDTs connected to an antenna, a shorted-grating reflector for a reference peak, and an IDT-type reflector linked to the GMI sensor. A change in impedance of the GMI sensor with respect to the external magnetic field gives rise to a variation in the reflection energy ($P_{11}(Z_{load})$) from the IDT-type reflector on the one-port SAW reflective delay line, according to the following equation^{36,37}.

$$P_{11}(Z_{load}) = P_{11}^{sc} + \frac{2P_{13}^2}{P_{33} + \frac{1}{Z_{load}}}$$

Here, P_{11}^{sc} is the acoustic reflection coefficient of the shorted-circuit IDT structure, P_{13} is the electroacoustic coupling factor, P_{33} is the electrical admittance of the IDT-type reflector, and Z_{load} is the load impedance that includes the GMI and the impedance of the capacitor installed for impedance matching. The variations in $P_{11}(Z_{load})$ caused by the external magnetic field result in a variation of the amplitude in the second reflection peak. By assessing the amplitude changes, the data about the current through the conductor line can be assessed.

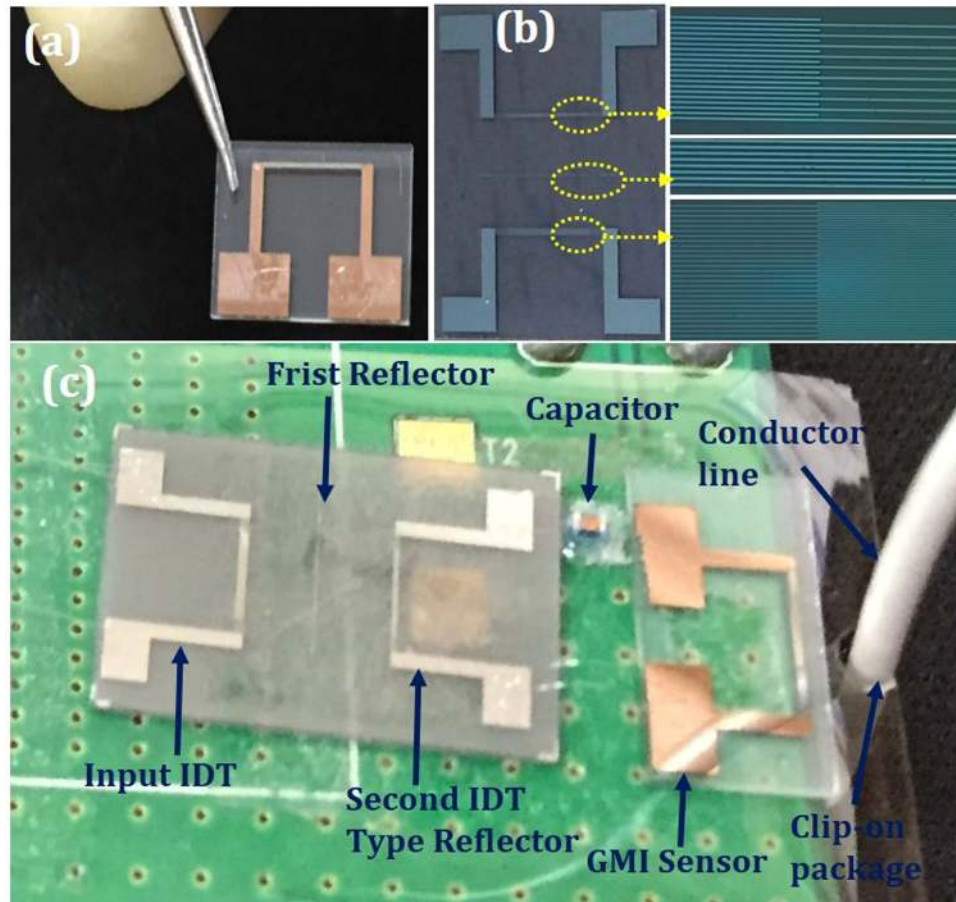


Figure 3. (a) View of the fabricated GMI sensor, (b) Overall and magnified views of the one port SAW reflective delay line, (c) Assembled units of all the devcies on clip-on packaging platform for wireless current sensing.

COM modeling was performed to obtain the results for the one port SAW reflective delay line in advance. A 41° YX LiNbO₃ piezoelectric substrate was chosen because it has a large electromechanical coefficient ($K^2 = 17\%$) and a high SAW velocity (~ 4000 m/s). The 400 MHz center frequency was selected, so that a reasonable antenna size could be used and also because the GMI sensor follows AC signals of ~ 400 MHz well. Thirty IDT finger pairs were selected and the aperture length was designed to be 40λ . Shorted grating bars were utilized for the reference reflector to induce higher reflectivity and lower insertion loss owing to the strong reflectivity and almost zero self-reflection, respectively. For the second reflector, an IDT-type reflector was chosen to convert the incoming SAW energy into AC signal for operating the GMI sensor.

Figure 2 shows the frequency and time response of the SAW delay line that were obtained by exploiting COM modeling. A sharp and narrow bandwidth peak was observed at 400 MHz center frequency region, as shown in Fig. 2(a), and two reflection peaks with high signal-to-noise ratio were observed in the time domain, as shown in Fig. 2(b). When the IDT-type reflector was simulated, the GMI sensor was treated as an inserted variable impedance source. Based on the disturbed impedance changes, the amplitude variations in the second reflection peak were extracted in terms of the external magnetic field generated by the current through the conductor, as shown in Fig. 2(b). COM simulations showed high sensitivity and good linearity in the amplitude variations.

To find the optimal capacitor in the system, simulation based on the following equation was carried out.

$$Z_{load} = R + j\omega L(H_{ext}) + 1/j\omega C_{match} \quad (2)$$

Here, R is the average resistance of the sensor, and $L(H_{ext})$ is the inductance of the GMI sensor in terms of the external magnetic field. Figure 2c shows the simulation results of the reflectivity of P_{11} as a function of the Z_{load} . The GMI sensor has an inductance range of 20–44 nH. From among the various capacitors, an 8 pF capacitor was chosen as the matching element and was connected in series with the GMI sensor owing to its highest reflectivity and good linearity in terms of the inductance. The ~ 8 pF capacitor was selected as the best matching element for different magnetic fields. The slope of the plot indicates the magnetic field sensitivity. With the optimal matching capacitance, a maximum reflectivity change rate of 0.67 dB/nH was observed.

Antenna. The surface current density in the patches was calculated to explain the radiation mechanism (Fig. 2d). Only the patches along the slit line were activated and they had a strong current across the direction of

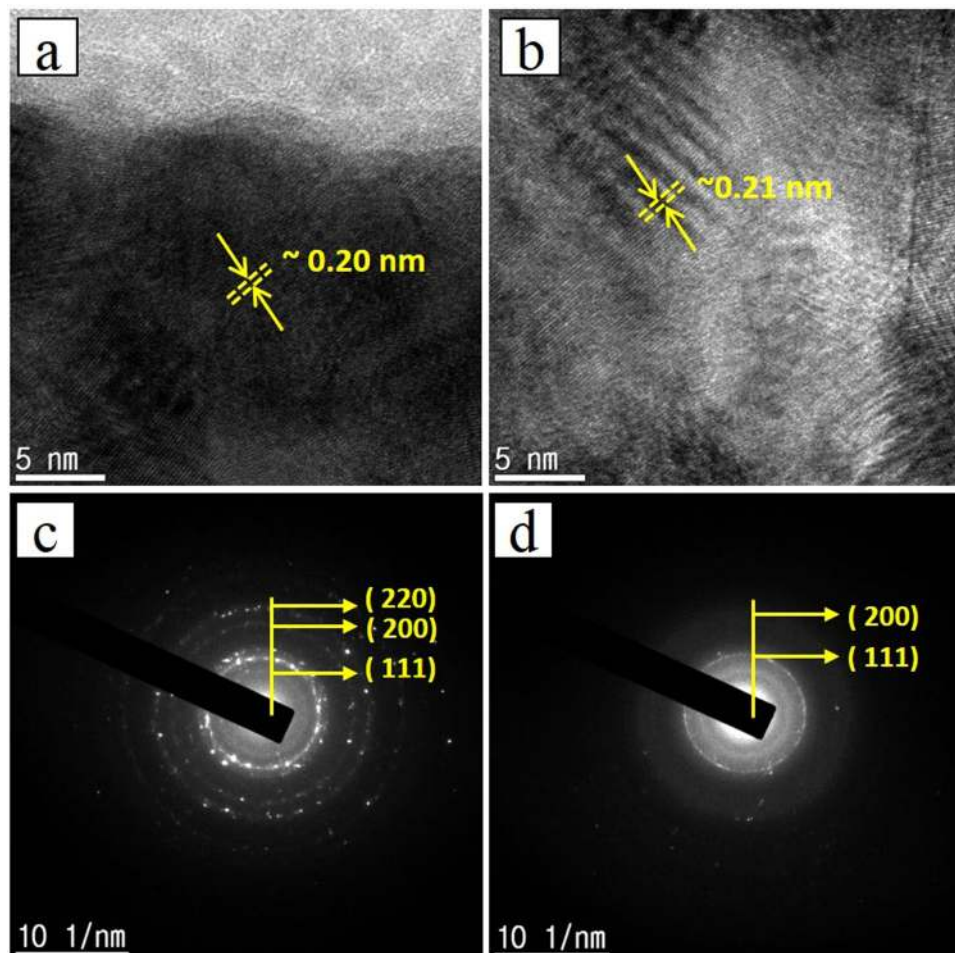


Figure 4. (a) HRTEM image of NiFe, (b) HRTEM image of Cu, (c) SAED pattern of NiFe, (d) SAED pattern of Cu.

the slit line (y-direction) that produced a strong field in the perpendicular direction. This outcome resulted in a wide beam width in the xz -plane and the antenna showed low back radiation. The antenna acts as a Yagi antenna with a director. Thus, the antenna radiates the majority of power in the direction of the strip. Figure 2e shows the 3-D radiation pattern of the antenna with the reference coordinate.

Fabricated devices. Figure 3 shows an overall view of the fabricated devices. For the GMI sensor, Cu was sandwiched between two soft magnetic material (NiFe) layers. The thickness of NiFe and Cu were 200 nm and 100 nm, respectively. The fabricated GMI sensor is shown in Fig. 3(a). The length and width of the GMI sensor along the stripe line were 2 mm and $\sim 150 \mu\text{m}$, respectively. Figure 3(b) shows the one-port SAW reflective delay line composed of the input IDT, shorted grating reflector, and IDT-type second reflector. For the input IDT, the number of finger pairs was 30, the finger width was $2.5 \mu\text{m}$, and the aperture length was 40λ . The first shorted-grating reflector was positioned 2.2 mm away from the input IDTs. The distance between the second reflector and the input IDT was ~ 4.6 mm. Figure 3(c) shows an overall view of the assembled units. The whole system is fixed to a conductor line with clip-on packaging platform and is secured to maintain the distance, angle, and tilt between the current-carrying conductor line and the GMI sensor.

GMI sensor. The high resolution transmission electron microscopy (HRTEM) analysis of the fabricated GMI sensor was performed to analyze the structural features as shown in Fig. 4(a,b). The HRTEM image reveals that the nanoparticles are densely distributed over the entire region in the NiFe and Cu layer. Figure 4a demonstrates that the lattice fringe spacing is about 0.20 nm in the NiFe layer, which is well indexed to the (111) plane of the cubic crystal structure of NiFe. The fringe spacing in the Cu layer was ~ 0.21 nm (Fig. 4b) which also well matched with the (111) plane of the cubic crystalline structure of Cu. The selected area electron diffraction (SAED) pattern displayed in Fig. 4(c,d) suggested a high crystal quality with a nanocrystalline nature of sputtered NiFe and Cu. Furthermore, the phase purity and crystal structure of the NiFe and Cu in the GMI device were investigated using the X-ray diffraction pattern. As shown in Fig. 5(a), the diffraction peaks of NiFe well agreed with the indices of the (111), (200), and (220) planes corresponding to the cubic crystal structure of NiFe, and the Cu diffraction peaks well agreed with the indices of the (111), (200), and (220) planes corresponding to the cubic crystal structure. The coercive forces and anisotropy field along the longitudinal magnetization direction were obtained

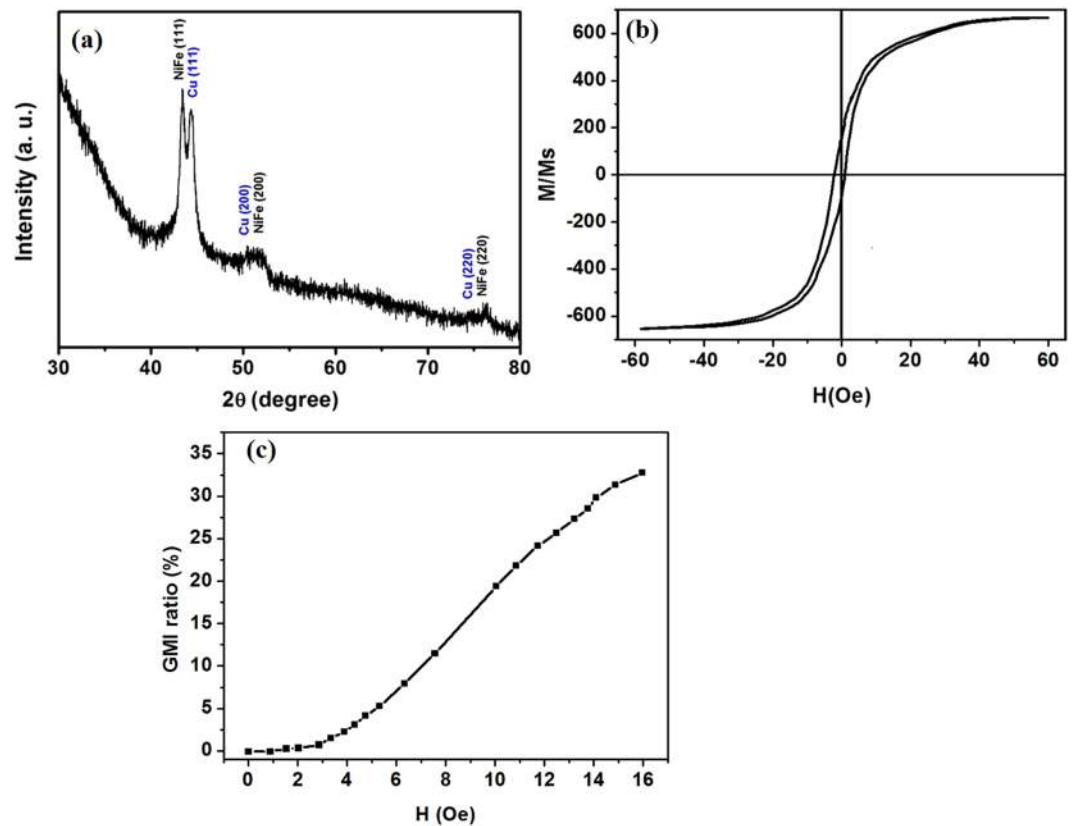


Figure 5. (a) X-ray diffraction pattern of the fabricated GMI magnetic sensor, (b) B-H curve of the GMI sensor, (c) Variation of GMI as a function of magnetic field.

by measuring the B-H curve. Figure 5(b) reveals a low coercive force, high anisotropy field, and low saturation induction indicating that the grown NiFe has a desirable soft ferromagnetic behavior. The coercive field strength (H_c) was ~ 1.28 Oe. The fabricated GMI sensor has a well-defined transverse magnetic anisotropy. In order to analyze the performance of the GMI sensor, a magnetic field H_{ex} was applied along its longitudinal direction. The magnetic field response of the GMI sensor was measured by an impedance analyzer shown in Fig. 5c. The GMI ratio was calculated from $Z(H)$ curves defined in the equation (3) below:

$$GMI \text{ ratio} = [Z(H_{ex}) - Z(H_0)]/Z(H_0) \times 100\%$$

where $Z(H_{ex})$ and $Z(H_0)$ are the magnetoimpedances in the presence and absence of an external magnetic field, respectively. The magnitude of the GMI increases up to 32.94% at 16 Oe. Further, sensitivity was calculated using the equation (4),

$$Sensitivity = [Z(H_2) - Z(H_1)/Z(H_1)]/(H_2) - (H_1) \times 100\%$$

The sensitivity was found to be 3.23%/Oe in magnetic fields of strength 3–16 Oe. The high sensitivity observed in the lower magnetic field region in the thin film GMI sensor makes it a better candidate for low-field magnetic sensing applications.

Chipless SAW transponder. Two antennas with center frequency of ~ 400 MHz were developed. One antenna was connected to the network analyzer while the other was connected to the input IDT of the SAW reflective delay line. The input RF power of ~ 1 mW was swept from 300 to 500 MHz, and the reflective scattering parameter S_{11} was measured in the frequency and time domains. A center frequency of 400 MHz was observed in the frequency domain (Fig. 6(a)), and S_{11} was sharp and had a narrow bandwidth. The experimental results were in good agreement with the COM modeling predictions with respect to the 400 MHz center frequency and the response shape. The reflective scattering parameter S_{11} obtained in the frequency domain was converted into the time domain as shown in Fig. 6(b). Two reflection peaks were observed with a large signal-to-noise ratio. The first reflection peak was observed at ~ 1.2 μ s, which was used as the reference peak. The second reflection peak appeared at 2.3 μ s and was connected to the GMI sensor via the impedance matching element. All the reflected peaks agreed well with the predicted values from the COM modeling in the frequency and time domain. The SAW delay line with and without the impedance matching element (8 pF capacitor) was compared to verify whether the impedance matching element lowers the insertion loss and increases the amplitude of the reflection peak. The second IDT-type reflector on the SAW delay line was linked to the GMI sensor by the 8 pF capacitor in

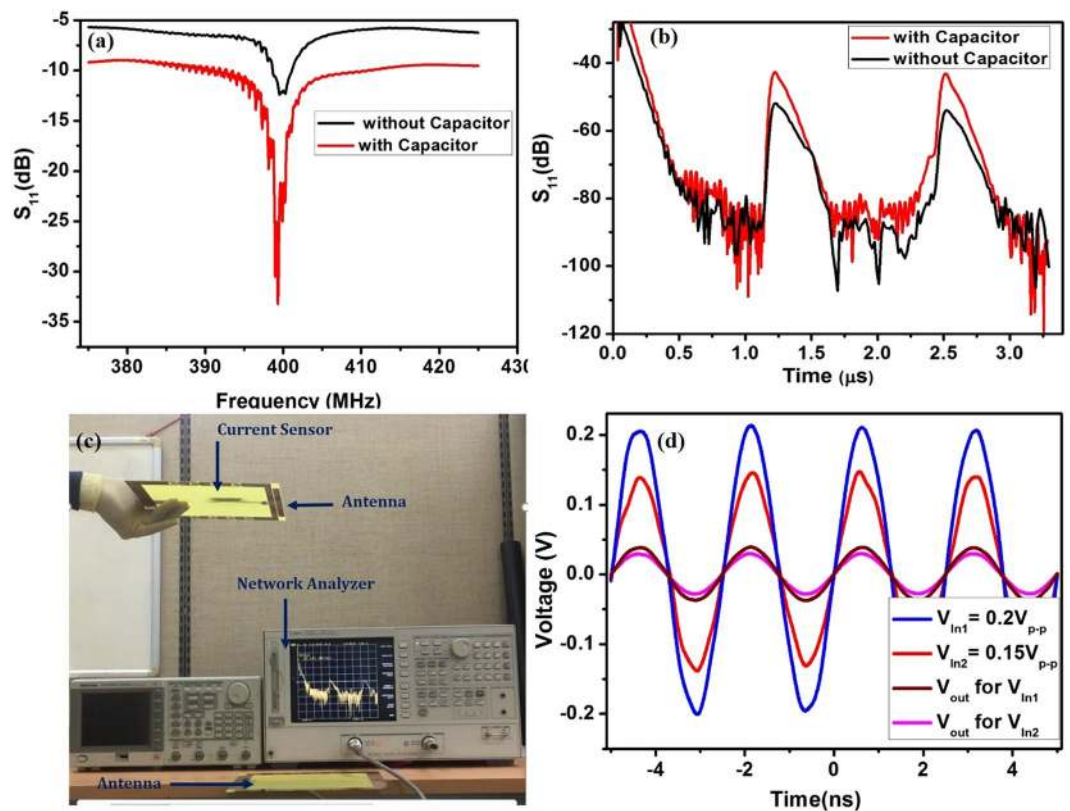


Figure 6. S_{11} response for one-port SAW reflective delay line with and without capacitor for impedance matching in (a) the frequency domain, (b) the time domain, (c) Wireless readout distance testing in terms of RF powers from the network analyzer, (d) AC voltages obtained from the second IDT-type reflector in terms of different input peak-to-peak voltages.

the middle. As shown in Fig. 6(a,b), the SAW delay line with the impedance matching element showed a lower insertion loss and higher signal to noise ratio when compared to the one without the impedance matching element. The center frequency and time positions of the reflectors were not changed, which is desirable for implementing the wireless, chipless current sensor system. The RF power from the network analyzer was changed to test the maximum reading distance (Fig. 6c). An increase in the applied RF power introduced a corresponding increase in the reading distance. With an RF power of 10 mW from the network analyzer, a readout distance of 5 m was observed. This reading distance can be further increased up to ~ 10 m by measuring the device under an EM shielded environment as given in ESI.

The GMI sensor was driven by AC signals generated from the second IDT-type reflector on the SAW reflective delay line; the IDT-type reflector converts the incoming SAW energy into AC signals. The AC voltages generated by the second IDT-type reflector were monitored using a high-frequency oscilloscope (Fig. 6d). A constant RF energy of 400 MHz was applied to the input IDT on the SAW delay line from a signal generator and the resultant output voltages at the IDT-type reflector were measured. AC signals with a range of ~ 0.05 $V_{\text{peak-to-peak}}$ were observed at the IDT-type reflector, which was used as the activation source for the GMI sensor. With an increase in the RF input power, there was a corresponding increase in the output peak-to-peak voltage, without any change in the frequency (Fig. 6d).

Wireless current sensing. A conducting line and the GMI sensor were fixed with the thick SU-8 polymer based clip-on packaging platform. The distance between the GMI sensor and conductor line was maintained at 2 mm. A constant DC of 1 A was passed through the conductor. The amplitude variation at the second reflection peak was observed due to the magnetic field generated by the flow of current that creates a magnetic spin orientation within the GMI device, leading to a change in the load impedance Z_{load} . Figure 7a shows a variation in the amplitude of the second reflection peak with an increase in the current through the conductor. The amplitude of S_{11} varied from -40.03 dB to -32.34 dB when the current through the conductor was increased from 1 A to 12 A. Here, the reading distance between the antennas and the input RF power were maintained constant as these parameters also affect the amplitude of the second reflection peak. The setting of a reference point at the amplitude of the second peak depends on the amplitude of the first reflection peak. The amplitude of the first peak was predicted based on the reading distance and the input RF power and the reference point at the amplitude of the second peak was determined based on the amplitude of the first peak. The variations in amplitude of the second reflection peak were re-plotted to obtain the sensitivity in terms of the current through the conductor, as shown

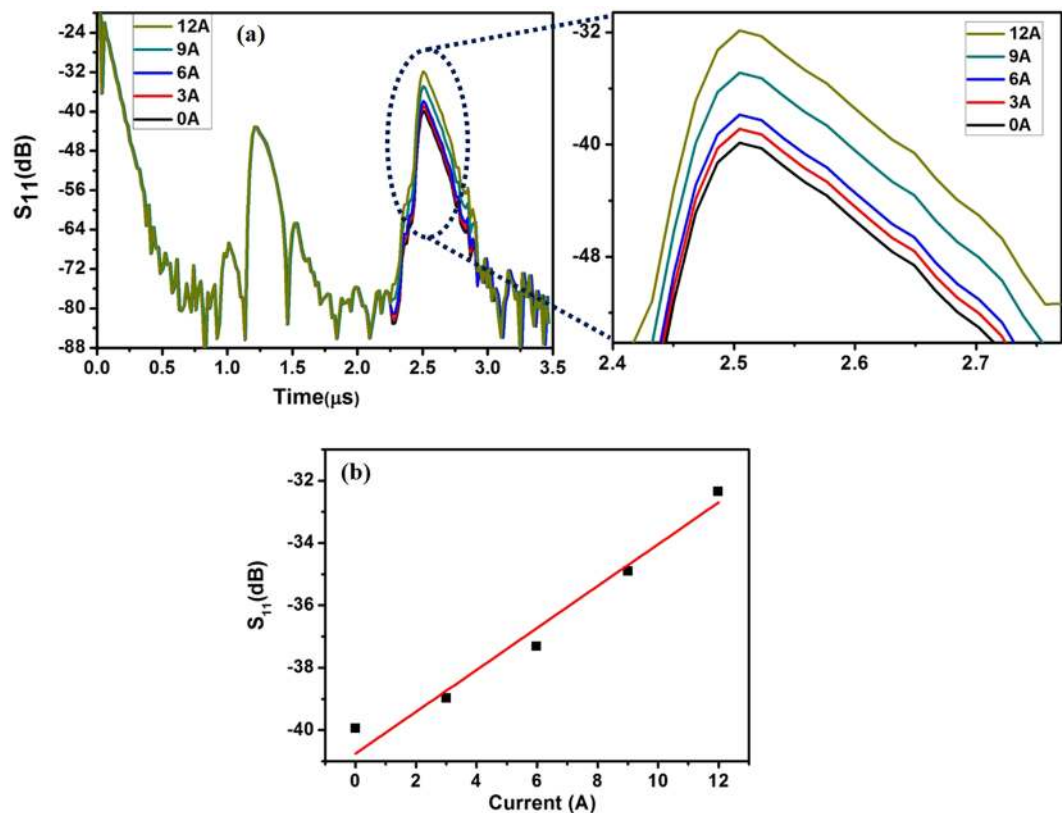


Figure 7. (a) Amplitude variations of the second reflection peak with respect to current flowing through conductor, (b) Calibrated amplitude variation of the sensor in terms of current flow in conductor line.

in Fig. 7b. Calibration was conducted to find the linearity and sensitivity. The sensitivity (S) of a sensor can be obtained using the equation (5)

$$S = \Delta S_{11}(\text{dB})/(\Delta A).$$

The highest sensitivity 0.691 dB/A was obtained and the linearity was found to be 0.962. The amplitude variations in the time domain, depending on the external current flow, were clearly observed; this is a promising result for the development of the battery-free, wireless sensor system.

Conclusions

This work creates a solid foundation for the development of a new configuration of current sensor system. For the first time, wireless current sensor system without transceiver system and interface circuitries were successfully designed, fabricated, and tested. This sensor system can eliminate currently complicated transceiver systems composed of thousands of electronic components and rechargeable heavy battery and can make battery-free, wireless measurements possible. A theoretical model for the prediction of a SAW amplitude variation with respect to the current flowing in the conductor was validated experimentally. A large variation in the amplitude of the reflection coefficient S_{11} was observed when the conductor carried a current. A sensitivity of 0.691 dB/A and a good linearity were observed for currents in the range 1–12 A. Our future work will be focused on integrating a voltage sensor with the current sensing system for monitoring the real-time power in a conductor.

Methods

GMI Sensor. A GMI sensor was developed on glass substrate using a DC sputter system. The magnetic alloy layer (NiFe) and the conducting layer (Cu) were deposited from elemental $\text{Ni}_{80}\text{Fe}_{20}$ and Cu targets respectively. The base pressure before sputtering was dropped to $\sim 1.5 \times 10^{-6}$ torr and the Ar gas pressure during the sputtering process was maintained at 3.5×10^{-3} torr. Each of the NiFe and Cu layers were sputtered successively from the respective targets under the same Ar gas pressure, and the deposition rates for NiFe and Cu were 2.0 $\text{\AA}/\text{s}$ and 5.0 $\text{\AA}/\text{s}$, respectively. A magnetic field of 150 Oe was applied perpendicular to the stripe length of the substrate holder during deposition to obtain a desirable magnetic anisotropy. For the desired width (150 μm) and length (2 mm) of the GMI sensor, a shadow mask was used during the sputtering process. The thicknesses of the NiFe and Cu layer were 200 nm and 100 nm, respectively. Schematic view of the fabrication of the GMI sensor via sputtering is shown in Fig. 8.

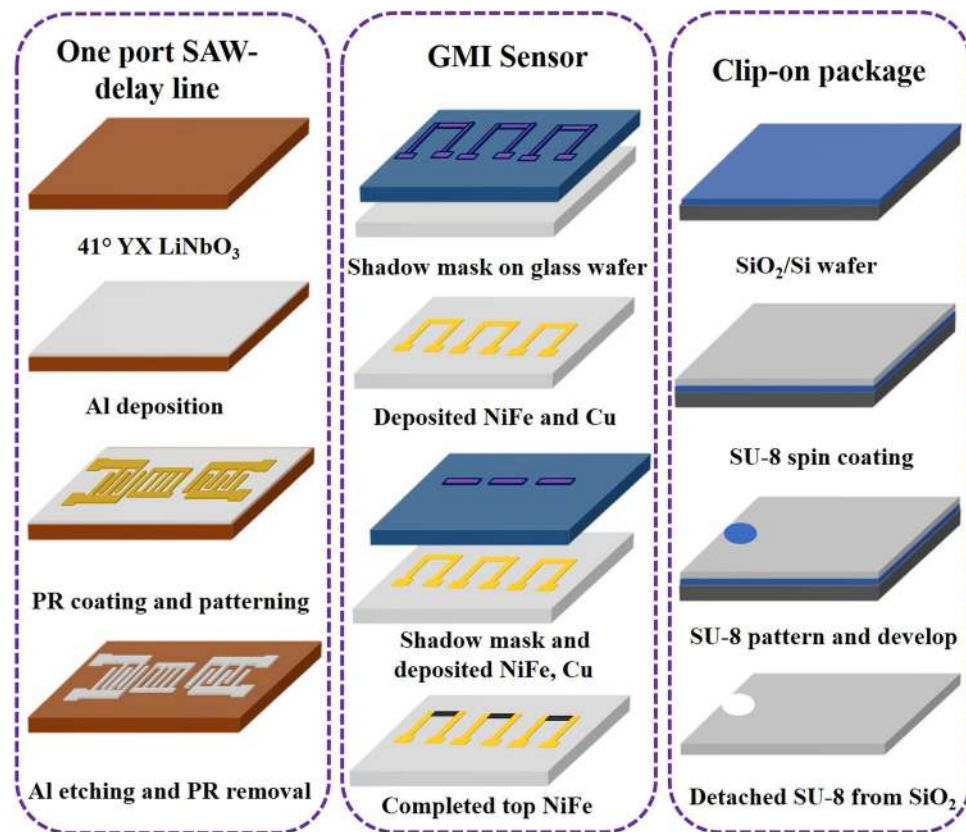


Figure 8. Schematic views of the fabrication procedures for one-port SAW reflective delay line, GMI sensor, and clip-on packaging platform.

SAW transponder. A 400 MHz one-port SAW reflective delay line was developed using the CMOS process. A 250 nm thick Aluminum (Al) layer was deposited on a 41° YX LiNbO₃ piezoelectric substrate using an e-beam evaporator and a 1 μm thick photoresist was then spin-coated on the wafer which was subsequently exposed and developed for the SAW transponder. The aluminum was wet-etched in a 4H₃PO₄:1HNO₃:4CH₃COOH:1H₂O solution and then the photoresist was removed in microstriper. It was rinsed several times with deionized water to eliminate the unwanted particles. The final devices were dicing-sawed to obtain the individual device, which were then wire-bonded with antenna pads. The detailed process for the fabrication of SAW devices is shown in Fig. 8.

Clip-on package platform. A clip-on package platform was fabricated using a thick SU-8 polymer to control the distance, angle, and tilt between the current-carrying conductor and the GMI sensor, as shown in Fig. 1. SU-8 polymer was spin-coated on a clean SiO₂/Si wafer to obtain a thickness of ~100 μm. The coated SU-8 polymer was soft-baked at 65 °C for 30 min and then at 95 °C for 10 min. Next, the SU-8 polymer layer was UV-exposed, post-baked at 65 °C for 15 min and then at 95 °C for 5 min. It was later developed to get a desired hole on the SU-8 platform. The ~100 μm thick flexible SU-8 polymer was detached from the SiO₂ wafer using buffered oxide etch (BOE) solution. The diameters of the holes were varied depending on the diameter of the conductor wire to be used.

Antenna and Unit assembly. A two-dimensional planar loop antenna with 400 MHz central frequency was fabricated using an 8-mm-thick FR4 substrate (dielectric constant $k = 3.38$). More details of antenna design are given in ESI. All the separately fabricated devices were put together to construct the chipless, wireless current sensor system. First, on the clip-on package platform, the GMI device, one-port-SAW reflective delay line, and the capacitor were assembled. The spacing between the center of the hole and the GMI sensor was maintained at 2 mm. The GMI was electrically connected to the corresponding IDT-type reflectors on the one-port SAW reflective delay line via an 8 pF capacitor in the middle. For wireless measurements, the two antennas were connected to the S₁₁ port of the network analyzer and the pads of the one-port SAW delay line. A conductor wire was clamped to the hole on the SU-8 package platform. The reflection coefficient S₁₁ was wirelessly measured in the time domain.

References

- Boonsong, W. & Ismail, W. Wireless Monitoring of Household Electrical Power Meter Using Embedded RFID with Wireless Sensor Network Platform. *Int. J. Distrib. Sens. N* **876914**, 1, <https://doi.org/10.1155/2014/876914> (2014).
- Ghayvat, H., Mukhopadhyay, S., Gui, X. & Suryadevara, N. WSN- and IOT-Based Smart Homes and Their Extension to Smart Buildings. *Sensors* **15**, 10350, <https://doi.org/10.3390/s150510350> (2015).
- Erol-Kantarci, M. & Mouftah, H. T. Wireless Sensor Networks for Cost-Efficient Residential Energy Management in the Smart Grid. *IEEE Trans. Smart Grid* **2**, 314, <https://doi.org/10.1109/TSG.2011.2114678> (2011).
- Suryadevara, N. K., Mukhopadhyay, S. C., Kelly, S. D. T. & Gill, S. P. S. WSN-Based Smart Sensors and Actuator for Power Management in Intelligent Buildings. *IEEE-ASME T Mech* **20**, 564, <https://doi.org/10.1109/TMECH.2014.2301716> (2015).
- Hancke, G. P., Silva, B. C. & Hancke, G. P. Jr The Role of Advanced Sensing in Smart Cities. *Sensors* **13**, 393, <https://doi.org/10.3390/s130100393> (2013).
- Visconti, P. & Cavalera, G. Intelligent System for Monitoring and Control of Photovoltaic Plants and for Optimization of Solar Energy Production. *IEEE Proc. of Int. Conf. Environment and Electrical Engineering* **1**, 1933, <https://doi.org/10.1109/EEEIC.2015.7165468> (2015).
- Visconti, P., Costantini, P. & Cavalera, G. Design of electronic programmable board with friendly touch screen interface for management and control of thermosolar plant parameters. *IEEE Conf. Proc. of Int. Conf. Environment and Electrical Engineering IEEEIC* **15310357**, 284, <https://doi.org/10.1109/EEEIC.2015.7165553> (2015).
- Bhatti, A. R., Salam, Z., Abdul Aziz, M. J. B. & Yee, K. P. A critical review of electric vehicle charging using solar photovoltaic. *Int. J. Energy Res.* **40**, 439, <https://doi.org/10.1002/er.3472> (2016).
- Lenz, J. & Edelstein, A. S. Magnetic sensors and their applications. *IEEE Sens. J.* **6**, 631, <https://doi.org/10.1109/JSEN.2006.874493> (2006).
- Gao, P., Lin, S. & Xu, W. A Novel Current Sensor for Home Energy Use Monitoring. *IEEE Trans. Smart Grid* **5**, 2021, <https://doi.org/10.1109/TSG.2013.2284760> (2014).
- Zhou, Q., He, W., Li, S. & Hou, X. Research and Experiments on a Unipolar Capacitive Voltage Sensor. *Sensors* **15**, 20678, <https://doi.org/10.3390/s150820678> (2015).
- Moghe, R., Iyer, A. R., Lambert, F. C. & Divan, D. M. A Low-Cost Wireless Voltage Sensor for Monitoring MV/HV Utility Assets. *IEEE Trans. Smart Grid* **5**, 2002, <https://doi.org/10.1109/TSG.2014.2304533> (2014).
- Bai, J. G., Lu, G.-Q. & Lin, T. Magneto-optical current sensing for applications in integrated power electronics modules. *Sens. Actuators A* **109**, 9, <https://doi.org/10.1016/j.sna.2003.09.038> (2003).
- Yang, X. *et al.* A Giant Magneto Resistive (GMR) Effect Based Current Sensor with a Toroidal Magnetic Core as Flux Concentrator and Closed-Loop Configuration. *IEEE Trans. Appl. Supercond.* **24**, 1, <https://doi.org/10.1109/TASC.2013.2286396> (2014).
- Xie, F., Weiss, R. & Weigel, R. Giant magnetoresistance based galvanically isolated voltage and current measurement. *IEEE Trans. Instrum. Meas.* **64**, 2048, <https://doi.org/10.1109/TIM.2015.2440553> (2015).
- Ray, W. F. & Davis, R. M. High frequency improvements in wide bandwidth Rogowski current transducers, *Proc. of EPE'99, Lausanne*, <https://doi.org/10.1080/09398368.1993.11463318> (1999).
- Ray, W. F. & Hewson, C. R. High performance Rogowski current transducers. *IEEE Industry Applications Conference* **5**, 3083, <https://doi.org/10.1109/IAS.2000.882606> (2000).
- Ward, D. A., La, J. & Exon, T. Using Rogowski coils for transient current measurements. *IEEE Engineering Science and Education Journal* **2**, 105, <https://doi.org/10.1049/esej:19930034> (1993).
- Xiao, C., Zhao, L., Asada, T., Odendaal, W. G. & Van Wyk, J. D. An overview of integratable current sensor technologies. *IEEE Industry Applications Conference*. <https://doi.org/10.1109/IAS.2003.1257710> (2004).
- Cubells-Beltrán, M.-D. *et al.* Integration of GMR Sensors with Different Technologies. *Sensors* **16**, 939, <https://doi.org/10.3390/s16060939> (2016).
- Li, B., Morsy, A. M. & Kosel, J. Optimization of Autonomous Magnetic Field Sensor Consisting of Giant Magnetoimpedance Sensor and Surface Acoustic Wave Transducer. *IEEE Trans. Magn.* **48**, 4324, <https://doi.org/10.1109/TMAG.2012.2202278> (2012).
- Pelegri, J., Ejea, J. B., Ramírez, D. & Freitas, P. P. Spin-valve current sensor for industrial applications. *Sens. Actuators A* **105**, 132, [https://doi.org/10.1016/S0924-4247\(03\)00091-8](https://doi.org/10.1016/S0924-4247(03)00091-8) (2003).
- Reig, C., Ramírez, D., Silva, F., Bernardo, J. & Freitas, P. Design, fabrication, and analysis of a spin valve based current sensor. *Sens. Actuators A* **115**, 259, <https://doi.org/10.1016/j.sna.2004.03.059> (2004).
- Reig, C., Ramírez, D., Li, H. H. & Freitas, P. P. Low current sensing with specular spin valve structures. *IEE Proc.-Circuits Devices Syst.* **152**, 307, <https://doi.org/10.1049/ip-cds:20050005> (2005).
- Reig, C., Cubells-Beltrán, M. D., Ramírez, D., Cardoso, S. & Freitas, P. P. Electrical Isolators Based on Tunneling Magnetoresistance Technology. *IEEE Trans. Magn.* **44**, 4011, <https://doi.org/10.1109/TMAG.2008.2002384> (2008).
- Kondalkar, V. V., Li, X., Yang, S. S. & Lee, K. Highly efficient current sensor built on a chip based on nanocrystalline NiFe/Cu/NiFe thin film. *J. Ind. Eng. Chem.* **53**, 416, <https://doi.org/10.1016/j.jiec.2017.05.014> (2017).
- Rowais, H. *et al.* Development of a passive and remote magnetic microsensor with thin-film giant magnetoimpedance element and surface acoustic wave transponder. *J. Appl. Phys.* **109**, 07E524, <https://doi.org/10.1063/1.3562041> (2011).
- Reig, C. & Ávila-Navarro, E. Printed Antennas for Sensor Applications: A Review. *IEEE Sens. J.* **14**, 2406, <https://doi.org/10.1109/JSEN.2013.2293516> (2014).
- Okada, H. & Itoh, T. Battery-less wireless current sensor node utilizing the dependence of charging time of a capacitor on the current flowing through a power line. *IEICE Electron. Express* **10**, 20130308, <https://doi.org/10.4236/wsn.2013.511026> (2013).
- Li, B., Salem, N. P. M. H., Giouroudi, I. & Kosel, J. Integration of thin film giant magnetoimpedance sensor and surface acoustic wave transponder. *J. Appl. Phys.* **111**, 07E514, <https://doi.org/10.1063/1.3678439> (2012).
- Fu, Q., Stab, H. & Fischer, W.-J. Wireless passive SAW sensors using single-electrode-type IDT structures as programmable reflectors. *Sens. Actuators A* **122**, 203, <https://doi.org/10.1016/j.sna.2005.05.006> (2005).
- Schimetta, G., Dollinger, F. & Weigel, R. A Wireless Pressure-Measurement System Using a SAW Hybrid Sensor, *IEEE Trans. Microw. Theory Techn.*, **48**, 2327, <https://doi.org/10.1109/22.899037> (2000).
- Li, B., Omar Yassine, O. & Kosel, J. A Surface Acoustic Wave Passive and Wireless Sensor for Magnetic Fields, Temperature, and Humidity *IEEE. Sensors J.* **15**, 453, <https://doi.org/10.1109/JSEN.2014.2335058> (2015).
- Jung, I. & Lee, K. Wireless neural probes based on one-port SAW delay line and neural firing-dependent varicap diode. *Sens. Actuators, B* **207**, 243, <https://doi.org/10.1016/j.snb.2014.10.070> (2015).
- Karilainen, A., Finnberg, T., Uelzen, T., Dembowski, K. & Muller, J. Mobile Patient Monitoring Based on Impedance-Loaded SAW-Sensors. *IEEE Trans. Ultrason., Ferroelect., Freq. Control* **51**, 1446, <https://doi.org/10.1109/TUFFC.2004.1367487> (2004).
- Steindl, R., Pohl, A., Reindl, L. & Seifert, F. SAW delay lines for wirelessly requestable conventional sensors. *Proc. IEEE Ultrasonics Symp.* **1**, 351, <https://doi.org/10.1109/ULTSYM.1998.762163> (1998).
- Reindl, L. & Ruile, W. Programmable reflectors for SAW-ID-tags. *Proc. IEEE Ultrasonics Symp.* **1**, 25, <https://doi.org/10.1109/ULTSYM.1993.339692> (1993).

Acknowledgements

This research work supported by the Korea Electric Power Corporation through Korea Electrical Engineering & Science Research Institute (Grant number: R15XA03–64) and Korea Institute of Energy Technology Evaluation and Planning (KETEP) (Grant number: 20172220200110).

Author Contributions

V.V.K. and K.K.L. contributed to the conception and design of the experiments, analysis of the data and writing the paper. V.V.K. carried out all experiments and wrote the paper. X.L. performed COM Modelling and calculations. I.P. fabricated the antenna. S.S.Y. participated in the scientific discussion and valuable suggestions during this manuscript. All authors discussed the results and reviewed the manuscript.

Additional Information

Supplementary information accompanies this paper at <https://doi.org/10.1038/s41598-018-20867-3>.

Competing Interests: The authors declare that they have no competing interests.

Publisher's note: Springer Nature remains neutral with regard to jurisdictional claims in published maps and institutional affiliations.



Open Access This article is licensed under a Creative Commons Attribution 4.0 International License, which permits use, sharing, adaptation, distribution and reproduction in any medium or format, as long as you give appropriate credit to the original author(s) and the source, provide a link to the Creative Commons license, and indicate if changes were made. The images or other third party material in this article are included in the article's Creative Commons license, unless indicated otherwise in a credit line to the material. If material is not included in the article's Creative Commons license and your intended use is not permitted by statutory regulation or exceeds the permitted use, you will need to obtain permission directly from the copyright holder. To view a copy of this license, visit <http://creativecommons.org/licenses/by/4.0/>.

© The Author(s) 2018